Turbulent mixing in supercritical jets: effect of compressibility factor and inflow condition

Nek Sharan* and Josette Bellan†
California Institute of Technology, Pasadena, California, 91125

Fuel injection and turbulent mixing at supercritical pressures determines ignition and combustion in numerous engineering applications. Flow evolution under such conditions is characterized by strong non-linear coupling between dynamics, transport coefficients, and thermodynamics. Experimental studies observe that the jets injected at supercritical pressures exhibit significantly different dynamics from the jets at subcritical conditions, owing to the lack of distinct liquid and gas phases in supercritical state. Thus, the averaged flow quantities such as the potential core length, jet spatial growth rate and velocity decay profiles differ in the two conditions, resulting in different mixed-fluid distributions. In this study, turbulent jet direct numerical simulations (DNS) are performed to examine the variations in flow statistics between injection of Nitrogen (N_2) in Nitrogen (N_2) at both subcritical (perfect-gas) and supercritical conditions. In all cases, isothermal round jets at Reynolds number (Re_D), based on jet diameter (D) and jet orifice velocity (U_0), of 5000 are considered. For mixing analyses, a passive scalar transported with the flow is examined.

I. Introduction

Combustion in numerous propulsion systems, *e.g.*, diesel, gas turbine, and liquid-rocket engines, occurs at pressures and temperatures that exceed the critical values of injected fuel and oxidizer. Pure species properties under supercritical conditions are significantly different from the properties at atmospheric conditions, a fact which influences flow dynamics, species mixing, and, as a result, power generation, soot formation, and thermal efficiency of the engines. Surface tension vanishes beyond the thermodynamic critical point, resulting in diffusion-driven mixing owing to no clear distinction between liquid and gas phases. Moreover, near the critical point several fluid properties, *e.g.,* density, constant-pressure specific heat, thermal conductivity and mass diffusivity, are highly sensitive to changes in pressure or temperature.

Detailed turbulence statistics at these high-pressure engine-relevant conditions, which may allow mixing or species concentration and its fluctuation estimates, are difficult to measure in experiments and, as of now, remain unavailable. Table 2 lists several experimental studies of supercritical round jets and the flow conditions considered in those experiments. All studies provide a qualitative assessment of the flow field, highlighting the challenge of obtaining high-fidelity measurements under these conditions. Additionally, the quantities to be measured and the location where they should be measured in order to capture the difference between atmospheric-pressure and high-pressure flows, are uncertain.

Numerical simulations can offer detailed flow and mixing statistics at high-pressure conditions. However, accurate simulations require careful choice of equation of state, mass and thermal diffusion models, and, at high-Reynolds-numbers, subgrid-scale models. To minimize model errors, direct numerical simulations of round-jet flows at Reynolds number, Re_D, based on jet diameter and exit velocity, of 5000 are performed in this study to model fuel injection. Equation of state and diffusion models described in Masi *et al.* [1] are employed for high-pressure simulations.

The effect of dynamics-based compressibility on shear layers, and turbulence in general, with respect to various (convective, turbulence, gradient, deformation) Mach numbers have been investigated at perfect-gas conditions in several previous studies[2–5]. An increase in dynamics-based compressibility results in reduction of turbulence levels and reduced momentum-thickness growth rate in shear layers. The reduction in turbulent kinetic energy is attributed to decrease in turbulent production resulting from reduced pressure fluctuations in the pressure-strain term[6]. Compressibility, as a result, also influences Reynolds stress components and associated anisotropy. Real-gas effects at high pressure introduce another type of compressibility, thermodynamics-based compressibility characterized by the compressibility factor, Z.

*now at CCS-2, Los Alamos National Laboratory, Member AIAA
†Jet Propulsion Laboratory, California Institute of Technology. Fellow AIAA.

Reference	Species (injected + chamber)	U_0 (m/s)	$T_{r,ch}$	$T_{r,inj}$	$P_{r,ch}$	$P_{r,inj}$	$Re_D \times 10^3$ $(\rho_{inj} U_0 D/\mu)$
Newman & Brzustowski (1971) [7]	$LCO_2 + CO_2/N_2$	2.0 - 4.0	0.97 - 1.09	0.97	0.86 - 1.23	NA	~ 20 - 30
Woodward & Talley (1996) [8]	$LN_2 + N_2$/He	~ 1.8 - 2.2	2.21 - 2.46	0.70 - 0.91	0.83 - 2.03	NA	3.4 - 4.1
Mayer *et al.* (1998) [9]	$LN_2 + N_2$	1	2.38	0.83	0.59 - 1.18	NA	~ 18 - 19
		1.3	1.98	0.71	0.83 - 2.03	NA	~ 21 - 23
	LN_2 + He	1.7	2.31	0.66	1.62 - 2.44	NA	~ 23 - 24
Oschwald & Schik (1999) [10]	$LN_2 + N_2$	5.0 - 20.0	2.36	0.79 - 1.11	1.17 - 1.76	NA	115 - 340
Chehroudi *et al.* (2002) [11]	$LN_2 + N_2$	10.0 - 15.0	2.38	0.71 - 0.87	0.23 - 2.74	NA	25 - 75
Mayer *et al.* (2003) [12]	$LN_2 + N_2$	1.8 - 5.4	2.36	1.0 - 1.11	3.95 - 5.98	NA	~ 47 - 157
Segal & Polikhov (2008) [13]	Fluoroketone + N_2	7.0 - 25.0	0.66 - 1.07	0.68 - 1.28	0.05 - 1.86	0.2 - 2.2	11 - 42
Roy *et al.* (2013) [14]	Fluoroketone + N_2	7.07 - 30.0	0.69 - 1.09	1.0 - 1.31	1.26 - 1.88	1.34 - 1.98	NA
Falgout *et al.* (2015) [15]	Dodecane + Air	NA	0.7 & 1.4	0.55	1.6 & 3.2	82.55	NA
Muthukumaran & Vaidyanathan (2016) [16, 17]	Fluoroketone + N_2	0.86 - 7.5	0.82 - 1.03	0.99 - 1.07	0.81 - 1.34	NA	NA
	Fluoroketone + He	0.82 - 19.0	0.82 - 1.05	0.98 - 1.07	0.72 - 1.34	NA	NA
Baab *et al.* (2016, 2018) [18, 19]	n-hexane + N_2	~ 91	0.58	1.24	1.65	1.81	120
	n-pentane + N_2	76 & 96	0.63	1.28 & 1.13	1.48	1.62 & 1.61	121 - 139
	Fluoroketone + N_2	41 & 72	0.67	1.13	1.34 & 2.11	2.11	172 - 272

Table 2 High-pressure round jet experimental studies. U_0 = jet-exit axial velocity, $T_{r,ch}$ = chamber reduced temperature, $T_{r,inj}$ = injectant reduced temperature, $P_{r,ch}$ = chamber reduced pressure, $P_{r,inj}$ = injectant reduced pressure, ρ_{inj} = injectant fluid density, NA = not available. ~ denotes values not provided in the reference but deduced from other parameters. Numbers in blue denote reduced chamber conditions based on injectant critical temperature and pressure.

Case (description)	$N_x \times N_y \times N_z$	p_∞ (bar)	$T_{\mathrm{ch}}\left(= T_{\mathrm{inj}}\right)$ (K)	Z	$\mathcal{F}$	Inflow perturbation
1 (atm-p)	$240 \times 216 \times 216$	1	293	1.0	6.5	$0.004U_0$ (lam)
	$320 \times 288 \times 288$					
	$400 \times 320 \times 320$					
2 (high-p (50); $Z \approx 1$)	$240 \times 216 \times 216$	50	293	0.99	309.4	$0.004U_0$ (lam)
	$320 \times 288 \times 288$					
	$400 \times 320 \times 320$					
	$480 \times 360 \times 360$					
3 (high-p (50); $Z \approx 0.9$)	$400 \times 320 \times 320$	50	199	0.9	641.4	$0.004U_0$ (lam)
	$480 \times 360 \times 360$					
4 (high-p (50); $Z \approx 0.8$)	$400 \times 320 \times 320$	50	170	0.8	895.7	$0.004U_0$ (lam)
	$480 \times 360 \times 360$					
	$560 \times 408 \times 408$					
5 (high-p (70); $Z \approx 0.9$)	$400 \times 320 \times 320$	70	211	0.9	774.1	$0.004U_0$ (lam)
	$480 \times 360 \times 360$					
1T (atm-p)	$400 \times 320 \times 320$	1	293	1.0	6.5	pipe-flow turb
2T (high-p (50); $Z \approx 1$)	$400 \times 320 \times 320$	50	293	0.99	309.4	pipe-flow turb

Table 3 Summary of the parameters for numerical simulations.

Turbulence statistics from jet-flow computations are sensitive to the choices of inflow/boundary conditions, domain size, and numerical discretization. In particular, the near-field flow development that determines the flame characteristics depends largely on inflow conditions. Experimental jet-flow studies typically use a smoothly contracting nozzle or a long straight pipe to initialize jet flows[20]. The contracting nozzle produces a laminar inflow with 'top-hat' velocity profile, whereas the long straight pipe produces a fully-developed turbulent inflow. The nature of perturbations characterized by its energy spectrum differ significantly in the two cases, a fact which has implications on both near- and far-field flow statistics.

II. Simulation setup and numerical details

Several flow cases, as outlined in Table 3, are considered to examine influences of high-pressure thermodynamics and inflow conditions on round-jet flows. Flow statistics at increasingly finer grid resolutions, denoted by $N_x \times N_y \times N_z$, in each case are compared to ensure grid convergence. In a first step, which is the present focus, single-species N_2 jets, which do not involve inter-species diffusion effects, at a Reynolds number of 5000 are simulated. In all cases, the injected and chamber fluid temperatures and pressures are the same, therefore, the jet injects into a chamber that is as dense as the injected fluid. Cases 2 to 4, as evident from Figure 1, investigate the effect of Z on fully-developed jet-flow turbulence as well as on the annular shear layer that forms in the early regions of jet-flow development. Case 5 examines the effects of pressure change, keeping compressibility factor Z constant, by comparisons against Case 3.

The role of initial/inflow conditions on free-shear flow development as well as the asymptotic (self-similar) state attained by the flow at atmospheric conditions is well recognized [21–23]. Cases 1T and 2T examine the influence of inflow perturbations on near- and far-field statistics at atmospheric and high-pressure conditions, respectively, by comparisons against Cases 1 and 2, respectively. The significance of factor $\mathcal{F}$ is explained in section II.A. Figure 1 shows Z, indicating deviation from perfect-gas behavior, of pure Nitrogen for a temperature range at 50 and 70 bar.

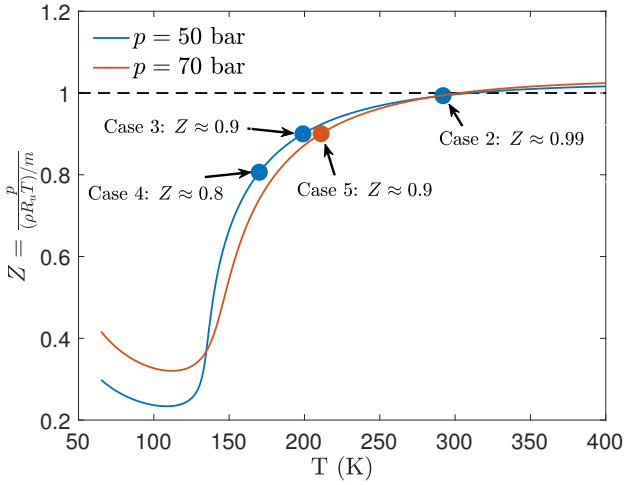

Fig. 1 Compressibility factor of N_2 at 50 and 70 bar pressure. Blue and red markers denote the chamber conditions for various cases of Table 3.

A. Governing equations

The compressible flow equations for conservation of mass, momentum, energy, and a passive scalar, solved in this study, are given by

$$\frac{\partial \rho}{\partial t} + \frac{\partial}{\partial x_j}\left[\rho u_j\right] = 0, \tag{1}$$

$$\frac{\partial}{\partial t}\left(\rho u_i\right) + \frac{\partial}{\partial x_j}\left[\rho u_i u_j + p\delta_{ij} - \sigma_{ij}\right] = 0, \tag{2}$$

$$\frac{\partial}{\partial t}\left(\rho e_t\right) + \frac{\partial}{\partial x_j}\left[\left(\rho e_t + p\right) u_j - u_i\sigma_{ij} + q_j\right] = 0, \tag{3}$$

$$\frac{\partial}{\partial t}\left(\rho \xi\right) + \frac{\partial}{\partial x_j}\left[\rho \xi\, u_j + J_j\right] = 0, \tag{4}$$

where t denotes the time, $(x_1, x_2, x_3) \equiv (x, y, z)$ are the Cartesian directions, subscripts i and j refer to the spatial coordinates, u_i is the velocity, p is the pressure, δ_{ij} is the Kronecker delta, $e_t = e + u_i u_i/2$ is the total energy (*i.e.*, internal energy, e, plus kinetic energy), $\xi \in [0, 1]$ is a passive scalar transported with the flow, σ_{ij} is the Newtonian viscous stress tensor

$$\sigma_{ij} = \mu\left(2S_{ij} - \frac{2}{3}S_{kk}\delta_{ij}\right), \qquad S_{ij} = \frac{1}{2}\left(\frac{\partial u_i}{\partial x_j} + \frac{\partial u_j}{\partial x_i}\right), \tag{5}$$

where μ is the viscosity, S_{ij} is the strain-rate tensor, and $q_j = -\lambda\, \partial T/\partial x_j$ and $J_j = -\mathcal{D}\, \partial \xi/\partial x_j$ are the heat flux and scalar diffusion flux in j-direction, respectively. λ is the thermal conductivity and $\mathcal{D} = \mu/Sc$ is the scalar diffusivity, where Sc denotes the Schmidt number. The injected fluid is assigned a scalar value, ξ, of 1, whereas the chamber fluid a value of 0. The passive scalar is not a physical species, and it is only used as a surrogate quantity to study mixing in this simple single-species flow; thus, the choice of the Sc value is arbitrary.

For the near-atmospheric-p simulation (Cases 1 and 1T), the perfect gas equation of state is applicable, given by

$$p = \frac{\rho R_u T}{m},$$

where R_u is the universal gas constant and m is the species molar mass. The viscosity is modeled as a power law

$$\mu = \mu_R \left(\frac{T}{T_R}\right)^n$$

with $n = 2/3$ and the reference viscosity $\mu_R = \rho_0 U_0 D/Re_D$, where ρ_0 and U_0 are the jet-exit fluid density and velocity, respectively, and the reference temperature $T_R = 293$ K. The thermal conductivity $\lambda = \mu C_p/\mathrm{Pr}$, where Prandtl number

Pr = 0.7 (as typical 1 bar flows), the ratio of specific heats $\gamma = 1.4$, and the isobaric heat capacity $C_p = \gamma R_u/(\gamma - 1)$ is assumed.

For the high-p simulations (Cases 2 to 5 and 2T), the governing equations (1)-(4) are closed using the Peng-Robinson (PR) equation of state (EOS)

$$p = \frac{R_u T}{(v_{PR} - b_{mix})} - \frac{a_{mix}}{\left(v_{PR}^2 + 2b_{mix}v_{PR} - b_{mix}^2\right)},$$

where the pressure, p, and temperature, T, are obtained as an iterative solution from the density, ρ, and internal energy, e, obtained from the conservation equations [24]. The molar PR volume $v_{PR} = v - v_s$, where the molar volume $v = m/\rho$. v_s denotes the volume shift introduced to improve the accuracy of the PR EOS at high pressures [24, 25]. a_{mix} and b_{mix} are obtained from the expressions detailed in past publications [26, Appendix B].

The physical viscosity, μ_{ph}, and thermal conductivity, λ_{ph}, are calculated using the Lucas method [27, Chapter 9] and the Stiel-Thodos method [27, Chapter 10], respectively. The computational viscosity, μ, and thermal conductivity, λ, are then obtained by scaling μ_{ph} and λ_{ph} with factor $\mathcal{F} = \mu_R/\mu_{ph,0}$, *i.e.*, $\mu = \mathcal{F}\mu_{ph}$ and $\lambda = \mathcal{F}\lambda_{ph}$, to simulate the flow at a specified Reynolds number Re_D; this choice ensures that the physical value of Pr is respected. The inflow physical viscosity, $\mu_{ph,0}$, is obtained from the Lucas method using the pressure p_∞ and the average temperature $\left(T_{inj} + T_{ch}\right)/2$, where the subscripts "inj" and "ch" denote the injection and chamber conditions, respectively.

To examine the robustness of the above EOS and transport coefficient models at supercritical conditions, Figure 2 compares the density, isobaric heat capacity, and the transport coefficients μ_{ph} and λ_{ph} obtained from the models against the National Institute of Standards and Technology (NIST) database [28] for N_2 at pressures of 50 and 70 bar and temperatures ranging from 100 K to 400 K. The supercritical temperature (T_c) of Nitrogen is 126.2 K. The transport coefficient models are accurate at supercritical temperatures only and, thus, their comparison spans values of $T > T_c$. As evident, the models have good agreement with the NIST database, showing their validity at high-p conditions encountered during simulations of Cases 2 to 5.

B. Numerical methods and computational domain

The spatial derivatives are approximated using the sixth-order compact finite-difference scheme and time integration uses the explicit classical fourth-order Runge-Kutta method. The outflow boundary in axial direction and all lateral boundaries have sponge zones[29] with non-reflecting outflow Navier-Stokes characteristic boundary conditions (NSCBC)[30] at the boundary faces. Sponge zones at each outflow boundary have a width of 10% of the domain length normal to the boundary face. The sponge strength at each boundary decreases quadratically with distance normal to the boundary. The performance of one-dimensional NSCBC[30] as well as its three-dimensional extension[31] by inclusion of transverse terms were also evaluated without the sponge zones; they permit occasional spurious reflections into the domain, therefore, the use of sponge zones was deemed necessary. To avoid unphysical accumulation of energy at the highest wavenumber, resulting from the non-dissipative spatial discretization, the conservative variables are filtered every five time steps using an eighth-order filter.

The computational domain extends to $42D_0$ in the axial (x-)direction and $20D_0$ in the y- and z-direction including the sponge zones, as shown in Figure 3.

C. Inflow condition

Cases 1 to 5 use a top-hat jet-exit mean velocity profile with random perturbations of small magnitude, as listed in Table 3, that models laminar inflow conditions, observed in jets exiting a smooth contracting nozzle [20]. The velocity profile at the inflow plane is given by [32]

$$u(r) = \frac{U_0}{2}\left(1 - \tanh\left[\frac{r - r_0}{2\theta_0}\right]\right),$$

where $r = \sqrt{y^2 + z^2}$, the jet exit radius $r_0 = D/2$ and the momentum thickness $\theta_0 = 0.04r_0$ is assumed. By choice, random perturbations with maximum amplitudes of $0.004U_0$ are superimposed on the inflow velocity profile to trigger jet flow transition to turbulence. No perturbations are added to fields other than velocity.

To model turbulent inflow conditions, typical of jets exiting a long pipe, the approach of Klein *et al.* [33], modified to accommodate circular-pipe inflow geometry, is used for cases 1T and 2T. The approach generates inflow statistics

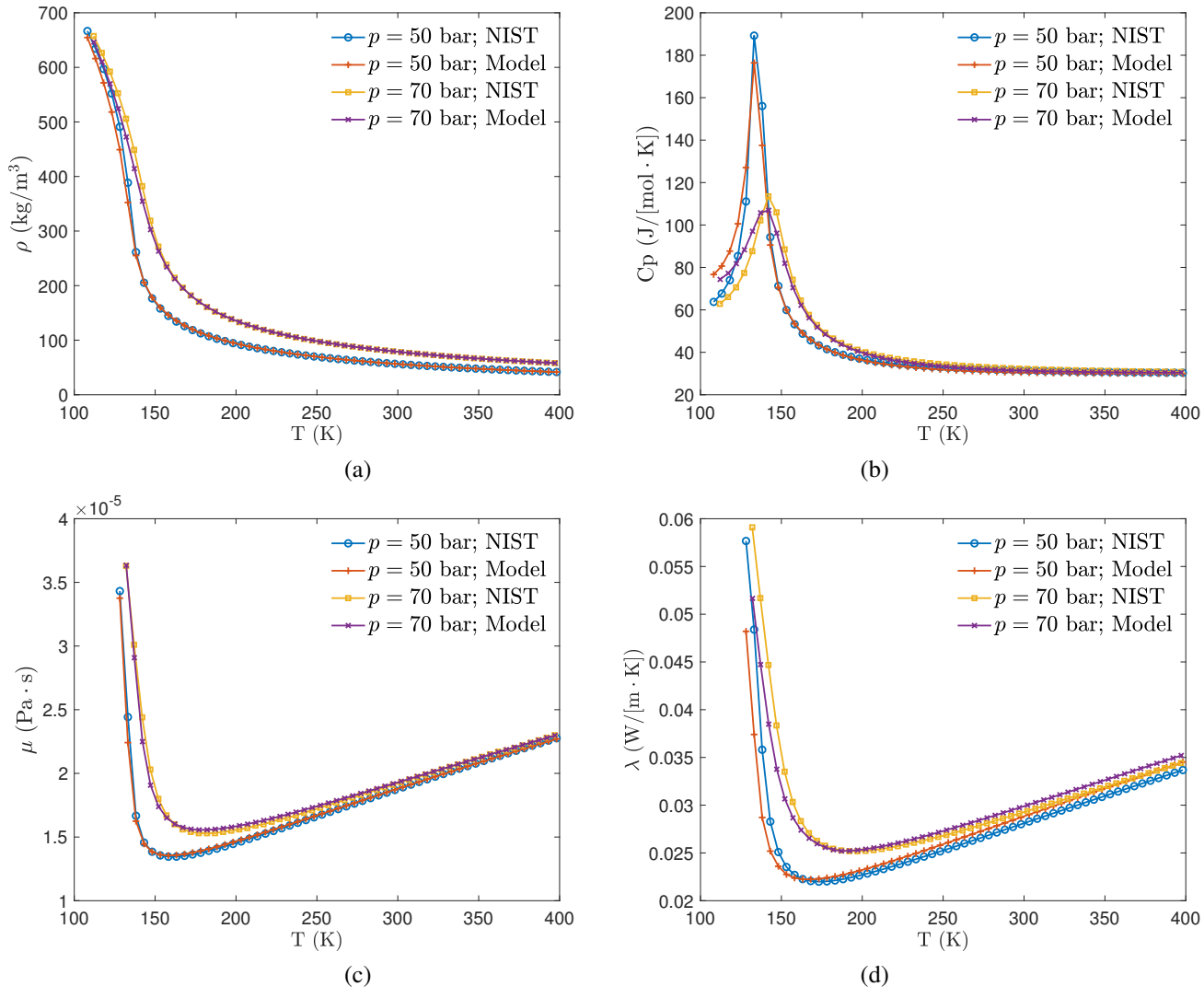

Fig. 2 EOS and transport coefficients model comparison against NIST database for pure Nitrogen at 50 bar pressure. (a) Density, (b) Isobaric heat capacity, (c) Viscosity, and (d) Thermal conductivity.

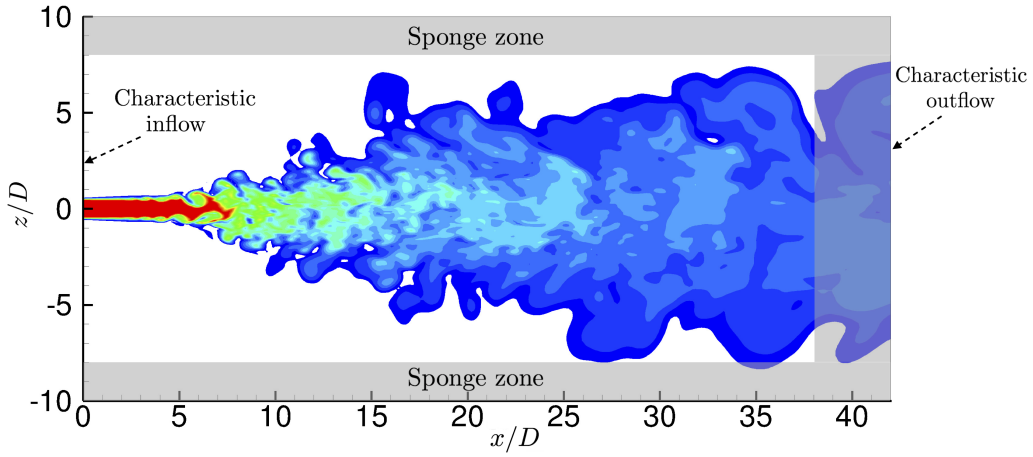

Fig. 3 A 2D schematic showing the extent of computational domain in axial and radial direction, and the boundary conditions applied at various boundaries.

matching a prescribed mean velocity and Reynolds stress tensor, using the method of Lund *et al.* [34], with fine-scale perturbations possessing a prescribed spatial correlation length scale. The mean velocity and Reynolds stress profiles are specified from the fully-developed pipe flow DNS results of Eggels *et al.* [35], where the Reynolds number, based on pipe diameter and bulk velocity, of 5300 is close to the jet Reynolds number of present study. The bulk velocity is defined as

$$U_b = \frac{1}{\pi\,(D/2)^2} \int_0^{D/2} 2\pi r u \,\mathrm{d}r.$$

The choice of correlation length scale determines the energy distribution among various scales. Increasing the length scale leads to more dominant large-scale structures. Since the turbulent inflow simulations are aimed at examining influences of fully-developed fine-scale inflow turbulence on jet statistics, a small isotropic value of $L/D = 0.1$ is assumed as the correlation length scale.

Figures 4 and 5 show a validation of the inflow implementation. Figure 4 compares the mean velocity from present inflow with the pipe flow DNS results (case DNS(E)) of Eggels *et al.* [35]. Figure 5 shows a similar comparison of the components of Reynolds stress tensor. $\langle\bullet\rangle$ denotes an average over time and azimuthal (θ) coordinate. The method described in Klein *et al.* [33] assumes a Cartesian grid with uniform spacing, where the periodic directions, along which averages are computed to determine mean quantities, are aligned with Cartesian directions. The inflow in a round jet, considered here, has circular orifice, where the azimuthal direction is periodic, which is not aligned with a Cartesian direction. Therefore, to compute statistics for comparisons, the azimuthal averages are computed by interpolation of time-averaged Cartesian-grid solution to a polar grid. Moreover, the filter coefficients used to generate spatially-correlated perturbations are appropriately modified to account for grid stretching in order to preserve the chosen correlation length scale.

D. Grid convergence

An estimate of the Kolmogorov length scale, η_K, can be made using the empirical relations of centerline velocity and jet's half-width, as described in [36], for incompressible flows. This length scale is then, commonly, used to obtain an estimate of the grid spacing required to perform a DNS. However, the relations for incompressible (or weakly compressible) flows may not apply in high-pressure flow regimes of interest here. Therefore, mean flow statistics are compared in this section by successively refining the grid for Cases 1 to 5 of Table 3 to ensure that sufficient grid points are used for the DNS.

Figures 6(a) to (e) compare the time-averaged centerline velocity, U_c, and scalar concentration, ξ_c, normalized by the jet exit values U_0 and ξ_0 as a function of axial distance from simulations of Cases 1 to 5 with various grid resolutions.

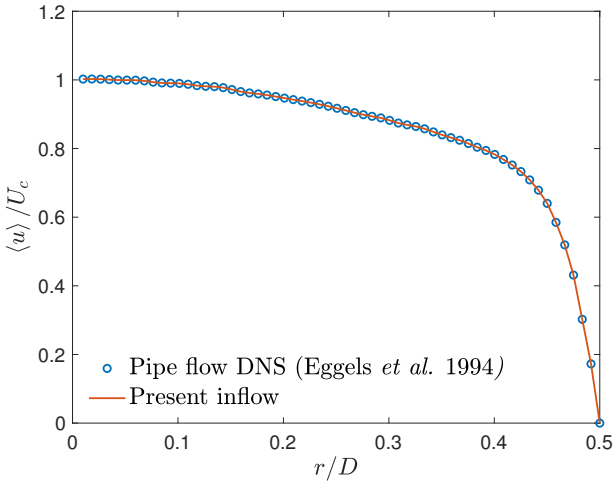

Fig. 4 Inflow mean velocity normalized by the centerline velocity for the (pseudo-)turbulent inflow compared against the pipe flow DNS results of [35].

Statistics for Case 1 at atmospheric conditions converges at a resolution of $320 \times 288 \times 288$, whereas, for high-pressure cases, they converge around $400 \times 320 \times 320$, except Case 4 at $Z = 0.8$ having maximum deviation from perfect gas among all cases considered that shows convergence around $480 \times 360 \times 360$. The plots also show that in all cases the scalar concentration begins to decay upstream of the velocity and at a faster rate than the velocity, consistent with the observation of Lubbers *et al.* [37, see Figure 6] for a passive scalar diffusing at unity Schmidt number.

III. Validation of atm-p simulation

Quantitative experimental data for supercritical jets is rare, however, numerous measurements of high-order statistics have been made for jets at atmospheric conditions. For comparisons, we consider here the measurements made in the self-similar region of the jet experiments by Wygnanski & Fiedler [38] and Panchapakesan & Lumley [39]. The Reynolds number of the Panchapakesan & Lumley experiments are closer to the Re_D of jets simulated in this study than the Wygnanski & Fiedler experiments. However, since the comparisons are made in the self-similar region and of quantities normalized by values specific to individual jets, data from both experiments can be used.

Figure 7 compares the decay of time-averaged centerline velocity normalized by the jet-exit velocity for Case 1 against decay slopes observed in the experiments. For a self-similar round jet with top-hat exit velocity profile, the centerline velocity $U_c\,(x)$ is given by the empirical relation[40]

$$\frac{U_c\,(x)}{U_0} = \frac{B}{(x - x_0)/D}, \tag{6}$$

where B is a constant and x_0 denotes the virtual origin. As evident from Figure 7(b), downstream of the potential core collapse, the time-averaged centerline velocity decays as inverse of the axial distance, where the rate of decay, given by B, is within the experimentally observed values of 5.7 and 6.06 by Wygnanski & Fiedler and Panchapakesan & Lumley, respectively.

Figure 9(a) shows the mean axial velocity normalized by the centerline velocity at various axial distances (shown in figure 8) as a function of similarity coordinates, compared against the self-similar profile from experiments. Mean quantities are obtained from a time average followed by an azimuthal average, given by a discrete approximation of

$$\bar{u} = \frac{1}{2\pi} \int_0^{2\pi} \left(\frac{1}{(t_2^* - t_1^*)} \int_{t_1^*}^{t_2^*} u(x, r, \theta, t) \mathrm{d}t \right) \mathrm{d}\theta. \tag{7}$$

The azimuthal averages are computed by interpolation of time-averaged Cartesian-grid solution to a polar grid at a given axial location. The radius of the polar grid at an axial location, x, is chosen as $0.4(x - x_0)$ to allow concentration of

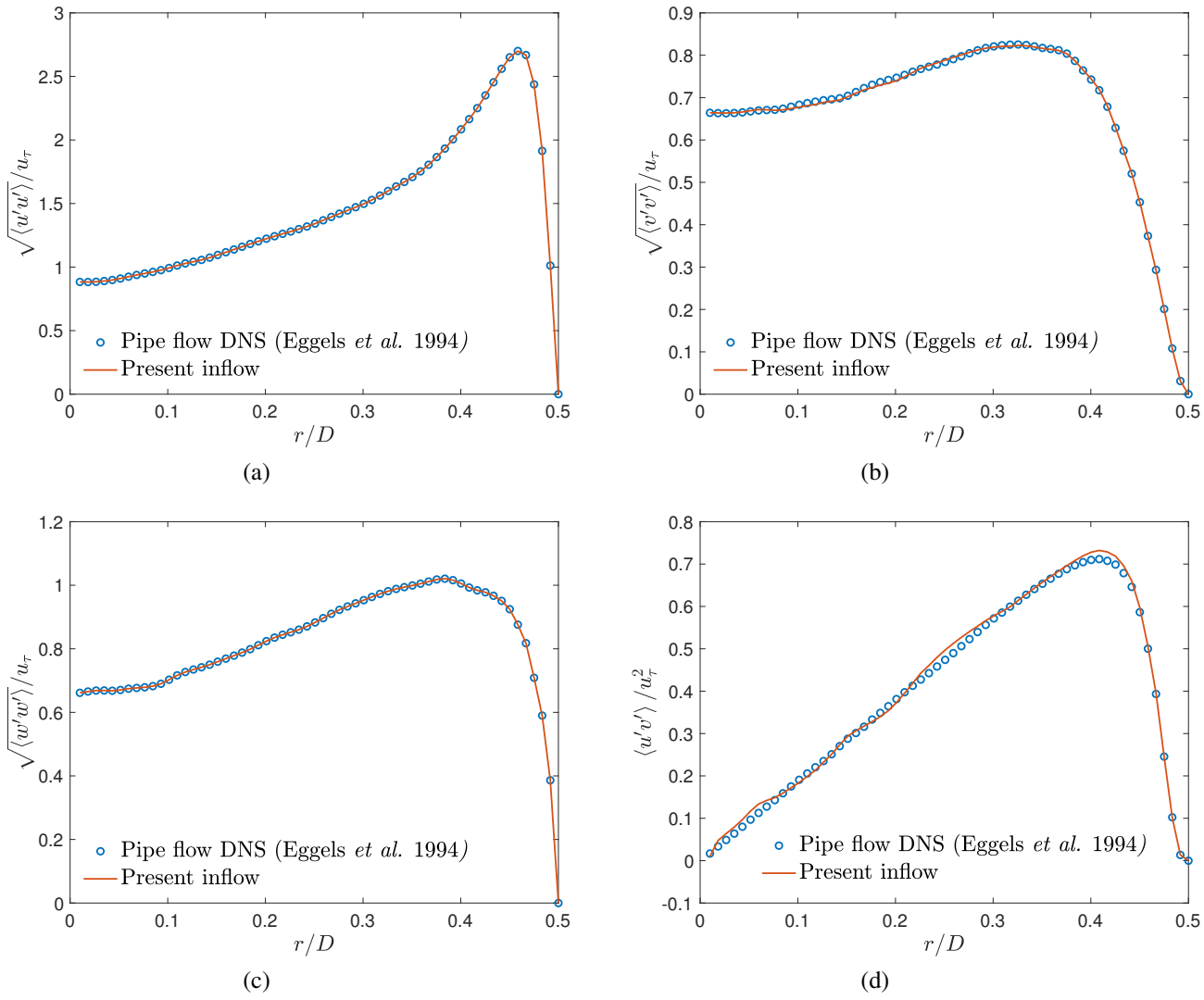

Fig. 5 Components of Reynolds stress tensor normalized by the wall friction velocity, u_τ, for the (pseudo-)turbulent inflow compared against the pipe flow DNS results of [35].

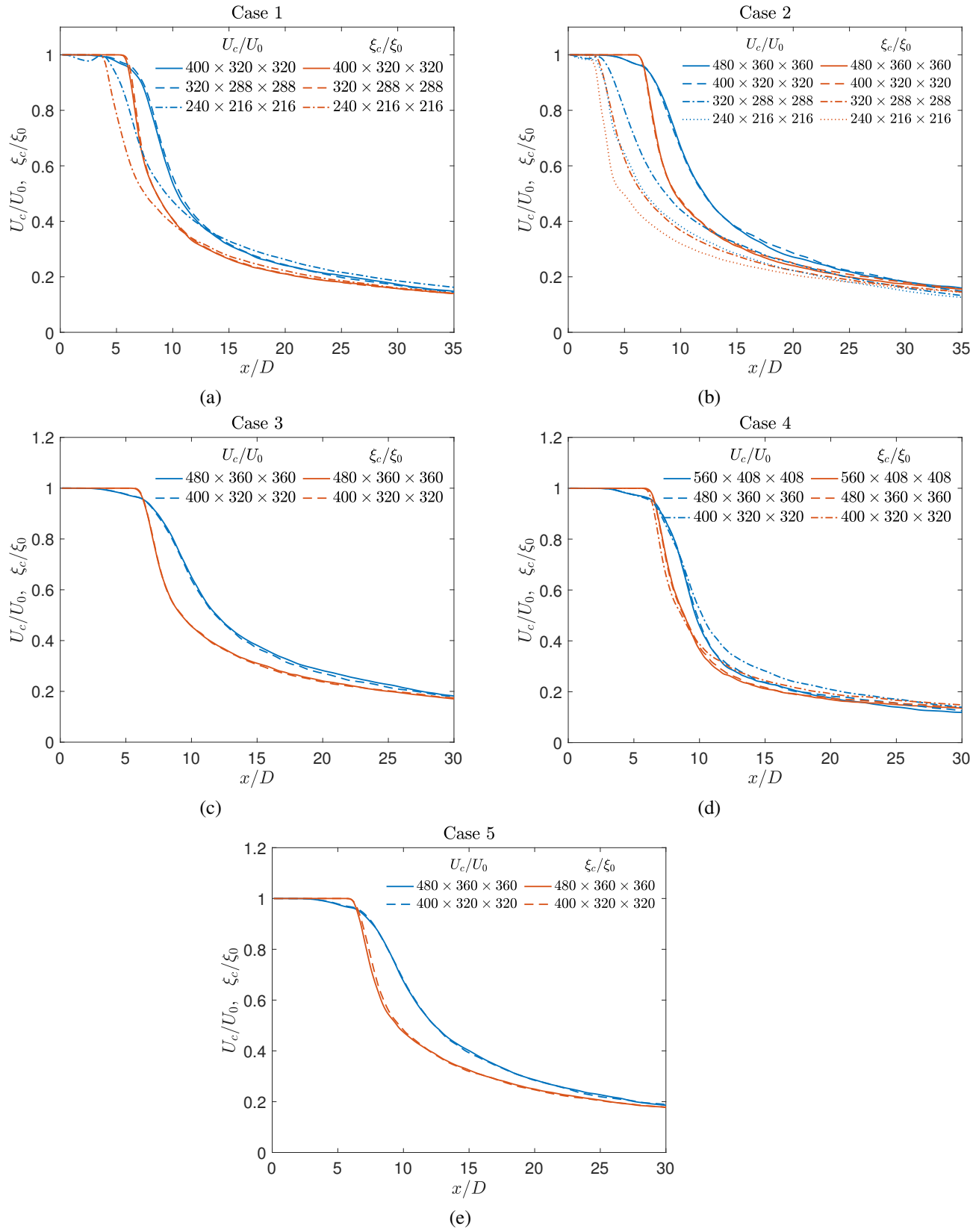

Fig. 6 Time-averaged centerline velocity (U_c) and scalar (ξ_c) values normalized by the jet exit values U_0 and ξ_0 as a function of axial distance for various grid resolutions. (a) Case 1, (b) Case 2, (c) Case 3, (d) Case 4, and (e) Case 5.

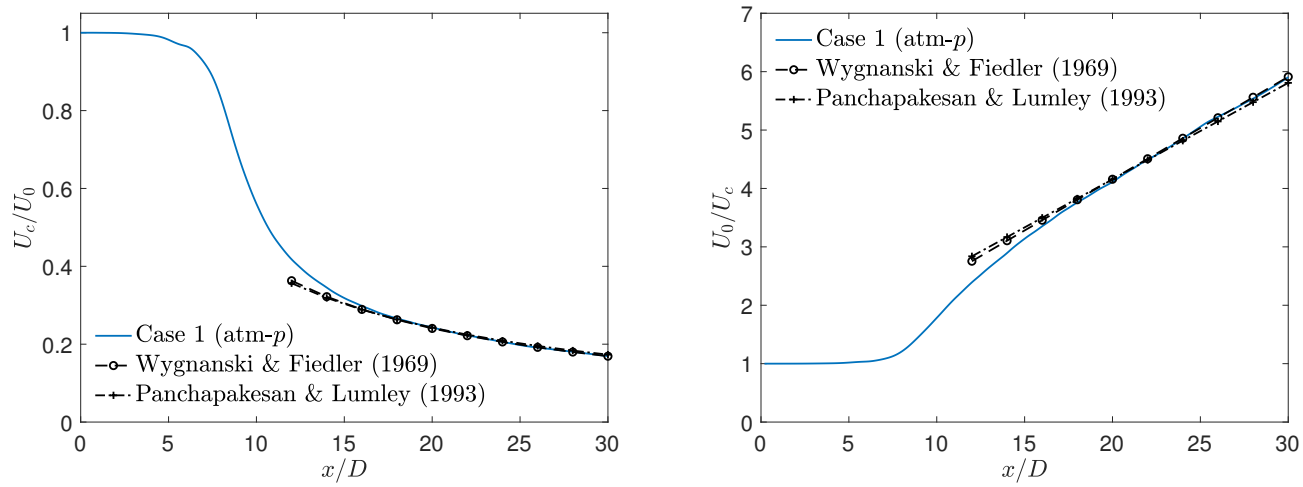

(a) (b)

Fig. 7 (a) Time-averaged centerline velocity (U_c) normalized by the jet-exit velocity U_0 as a function of axial distance and (b) inverse of the normalized time-averaged centerline velocity showing linear decay asymptotically with axial distance, compared against the decay slopes observed in [38, 39].

polar grid points inside the jet, where $x_0 = 4D$ is assumed. The polar grid has 60 grid points each in the azimuthal and the radial direction. The time average is performed over all time steps in the interval $t_1^* = 1000 \leq tU_0/D \leq 5000 = t_2^*$.

Figure 9(b) shows the normalized axial velocity r.m.s. fluctuations compared against the self-similar profile from experiments. The axial velocity r.m.s. fluctuation is calculated from

$$u'_{\text{rms}} = \left\langle \sqrt{\left\langle (u - \langle u \rangle_t)^2 \right\rangle_t} \right\rangle_\theta = \left\langle \sqrt{\left\langle u^2 \right\rangle_t - \langle u \rangle_t^2} \right\rangle_\theta, \tag{8}$$

where $\langle \cdot \rangle_t$ denotes time averaging and, similarly, $\langle \cdot \rangle_\theta$ denotes azimuthal averaging. Using this notation, (7) can be written as $\bar{u} = \langle \langle u \rangle_t \rangle_\theta$. At the centerline, there is no azimuthal averaging, therefore, using $\bar{u} = \langle u \rangle_t = U_c$, equation (8) becomes

$$u'_{c,\text{rms}} = \sqrt{\left\langle (u - U_c)^2 \right\rangle_t} = \sqrt{\left\langle u^2 \right\rangle_t - U_c^2}. \tag{9}$$

Both the mean and the r.m.s. axial velocity fluctuations agree well with the respective self-similar profiles from experiments. The mean axial velocity achieves self-similarity by $x/D \approx 15$, whereas the r.m.s. fluctuations do not attain self-similarity until after $x/D \approx 20$.

IV. Effects of inflow condition

Statistics between cases using the laminar top-hat inflow velocity profile (Cases 1 and 2) and those using the (pseudo-)turbulent fluctuations that match various statistics of a pipe-flow turbulence (Cases 1T and 2T), as described in section II.C, are discussed here. The jet flow from laminar inflow conditions, typical of jets exiting a smooth contracting nozzle, are characterized by large-scale coherent structures that extend to the far field. In contrast, coherent structures are only intermittently observed in the far field of a jet from turbulent pipe inflow [20].

Figure 10 compares the normalized time-averaged centerline velocity between the various cases. The potential core length differs between the cases of laminar and (pseudo-)turbulent inflow. However, the asymptotic velocity decay rate for all cases are similar. For laminar inflow, a comparison between the atmospheric- (Case 1) and high-pressure (Case 2) results shows that the velocity decay in the transition region is lower in the latter case.

Figure 11 shows the normalized r.m.s. velocity and scalar fluctuations along the centerline from the two inflows, calculated using equation (9). In addition to differences in potential core length that can, perhaps, be modulated by inflow

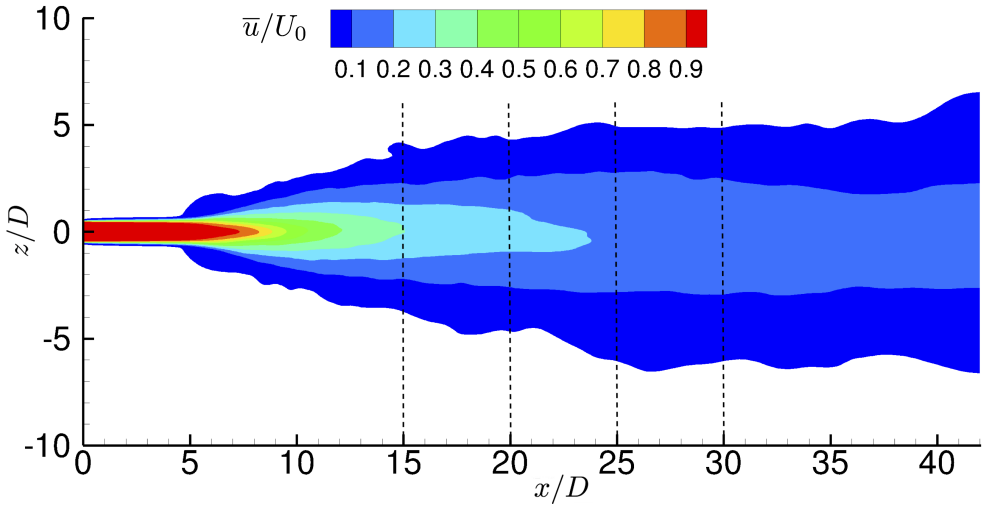

Fig. 8 Time-averaged axial velocity contours for Case 1. The dashed lines show axial locations where statistics are azimuthally averaged for figure 7.

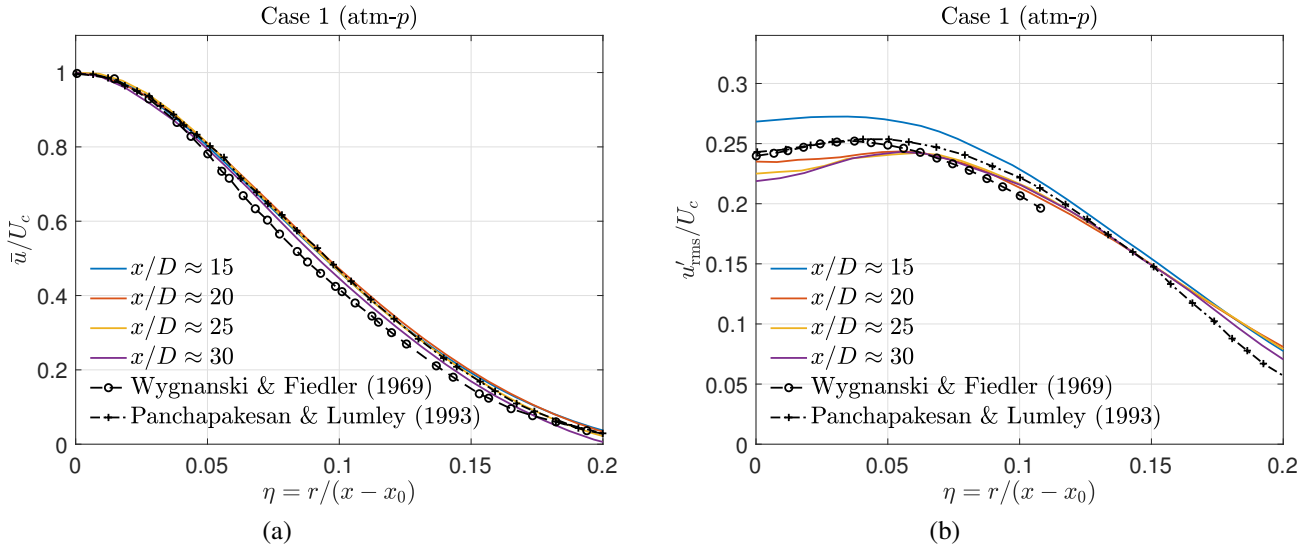

Fig. 9 (a) Mean axial velocity, $\bar{u}$, and (b) r.m.s axial velocity fluctuations, u'_{rms}, normalized by the centerline velocity at various axial distances plotted as a function of similarity coordinates.

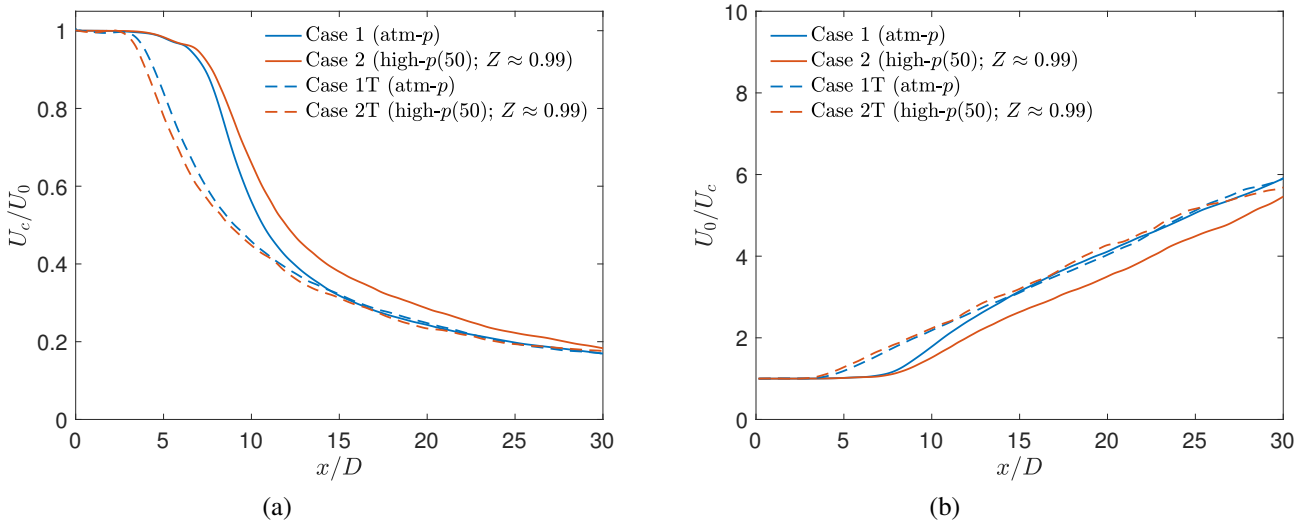

Fig. 10 Comparison between cases of laminar and (pseudo-)turbulent inflow. (a) Time-averaged centerline velocity (U_c) normalized by the jet-exit velocity, U_0, as a function of axial distance and (b) inverse of the normalized time-averaged centerline velocity.

perturbation magnitude in laminar inflow, there are significant differences between the statistics from the two inflows. The strong hump downstream of the potential core collapse, indicating significantly higher fluctuations, occurs in cases of laminar inflow but not in cases of (pseudo-)turbulent inflow. This is consistent with the experimental observations of Mi *et al.* [20, see Figure 17]. A comparison between figures 11(a) and (b) suggests that the velocity fluctuations are more sensitive to pressure differences than the scalar fluctuations, especially in the transition region downstream of potential core collapse. Moreover, the differences are higher for laminar inflow cases, which have large-scale organized structures. The sensitivity of velocity fluctuation is expected from the presence of pressure term in the momentum equation. The scalar fluctuations, normalized by the centerline value, asymptote to a value of around 0.2 for all cases within the axial distance of 30D, however, the normalized velocity fluctuations continue to show significant variations.

Figure 12 compares the axial velocity profiles as a function of similarity coordinate at various axial locations, marked in figure 8. For a given simulation, the profiles at various axial locations match quite well, a fact which suggests that the self-similar state has been attained in each case. However, the self-similar states differ from each other since, in both figures 12(a) and (b), the profiles from laminar inflow (solid lines) do not match with the profiles from (pseudo-)turbulent inflow (dashed lines). This suggests that the asymptotic state attained by the jet flow depends on the inflow condition, consistent with the theoretical [41] and experimental [20] results at atmospheric pressure; for supercritical pressure, this finding constitutes a new result.

V. Effects of compressibility factor

Comparison of the statistics from Cases 1 to 5 examines the influence of Z for laminar inflow. Figure 13 shows the time-averaged centerline velocity normalized by the jet-exit velocity as a function of axial distance. As observed in the previous section, the transition region is more sensitive to pressure changes. Therefore, though the potential core collapse in each case occurs approximately at the same axial distance, the decay rates in the transition region vary significantly. It will be interesting to see if this sensitivity is specific to laminar inflows, and whether it also occurs for turbulent inflows, a subject which will be addressed in future investigation.

Figure 14 compares the normalized r.m.s. velocity and scalar fluctuations along the centerline for various laminar inflow cases. As noted in the previous section, the velocity fluctuations show higher sensitivity to pressure changes than the scalar fluctuations, indicating that the former would be crucial information to acquire experimentally.

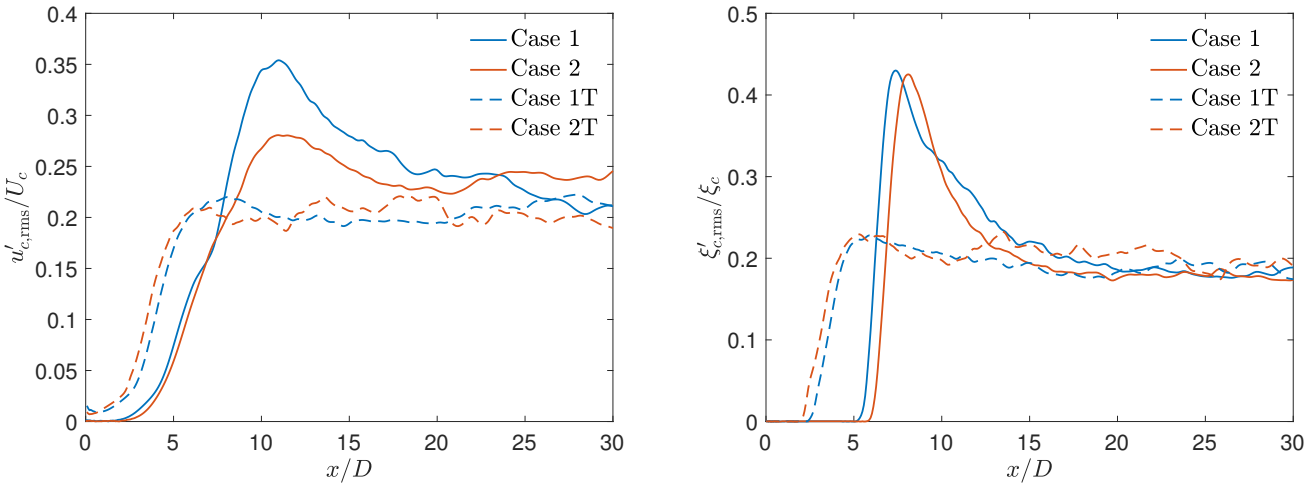

Fig. 11 Comparison between cases of laminar and (pseudo-)turbulent inflow. (a) Centerline r.m.s. axial velocity fluctuation and (b) centerline r.m.s. scalar fluctuation, normalized by the respective centerline values.

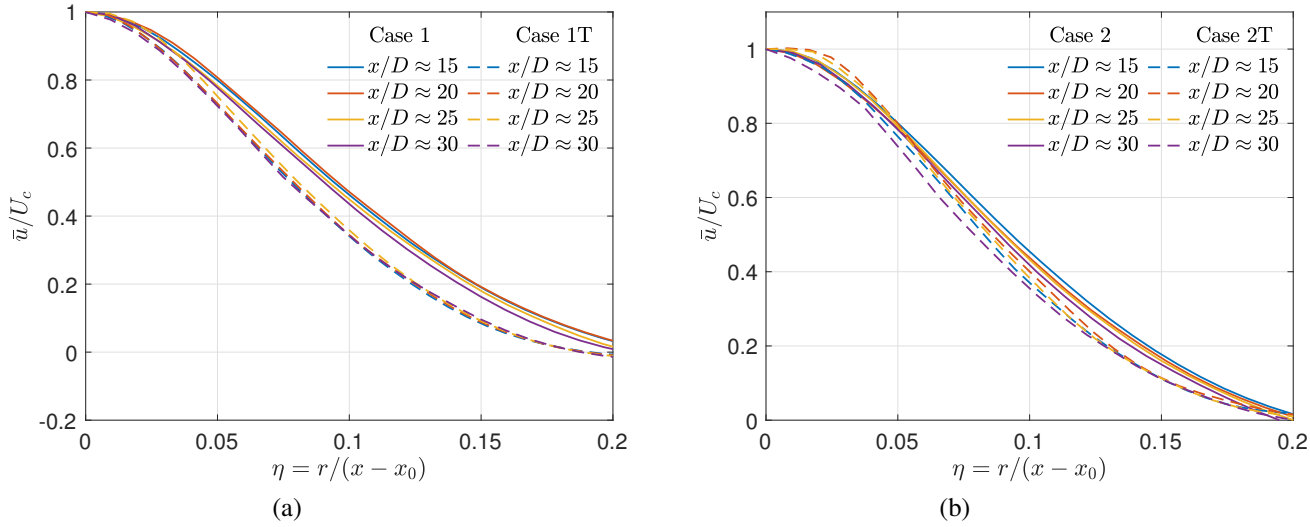

Fig. 12 Normalized mean axial velocity plotted as a function of similarity coordinates. Comparison between (a) Case 1 and 1T and (b) Case 2 and 2T.

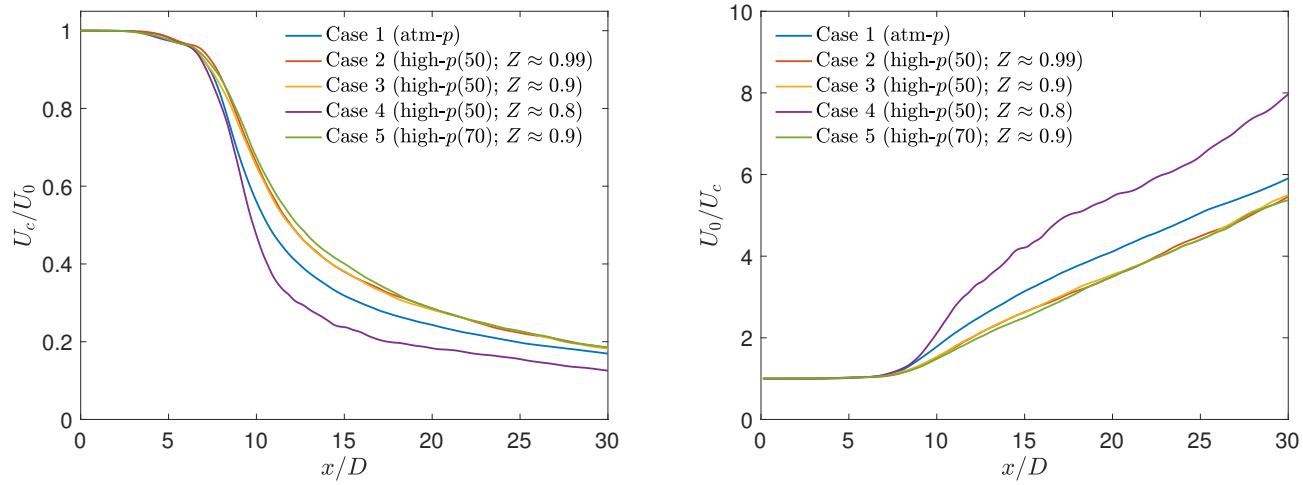

Fig. 13 Comparison between Cases 1 to 5. (a) Time-averaged centerline velocity (U_c) normalized by the jet-exit velocity U_0 as a function of axial distance and (b) inverse of the normalized time-averaged centerline velocity.

VI. Conclusions

Turbulent jet simulations at various chamber and inflow conditions are performed as part of an effort to understand fuel injection and mixing at high pressures. Both perfect gas (subcritical) and real gas (supercritical) conditions are considered to understand the differences in dynamics caused by the specified chamber pressure. The equation of state and transport coefficient models are accordingly chosen for the two conditions. For supercritical pressures, the transport property models are validated against the NIST database. To assess the influence of inflow conditions, a laminar inflow with top-hat velocity profile (and small random perturbations) and a (pseudo-)turbulent inflow with statistics matching pipe-flow turbulence data is considered. The state of the inflow condition influences flow statistics both in the near-field, containing potential core collapse and transition region, and the far-field, containing fully-developed flow with self-similar statistics, at both atmospheric as well as high pressures. The sensitivity to inflow and pressure conditions is higher in the transition region, where pressure changes significantly influence velocity fluctuations in the laminar-inflow jet, which has dominant large-scale coherent structures.

Acknowledgments

This work was supported by the Army Research Office under the direction of Dr. Ralph Anthenien. The computational resources were provided by the NASA Advanced Supercomputing at Ames Research Center under the T^3 program directed by Dr. Michael Rogers.

References

[1] Masi, E., Bellan, J., Harstad, K. G., and Okong'o, N. A., "Multi-species turbulent mixing under supercritical-pressure conditions: modelling, direct numerical simulation and analysis revealing species spinodal decomposition," *Journal of Fluid Mechanics*, Vol. 721, 2013, pp. 578–626.

[2] Papamoschou, D., and Roshko, A., "The compressible turbulent shear layer: an experimental study," *Journal of fluid Mechanics*, Vol. 197, 1988, pp. 453–477.

[3] Lele, S. K., "Compressibility effects on turbulence," *Annual review of fluid mechanics*, Vol. 26, No. 1, 1994, pp. 211–254.

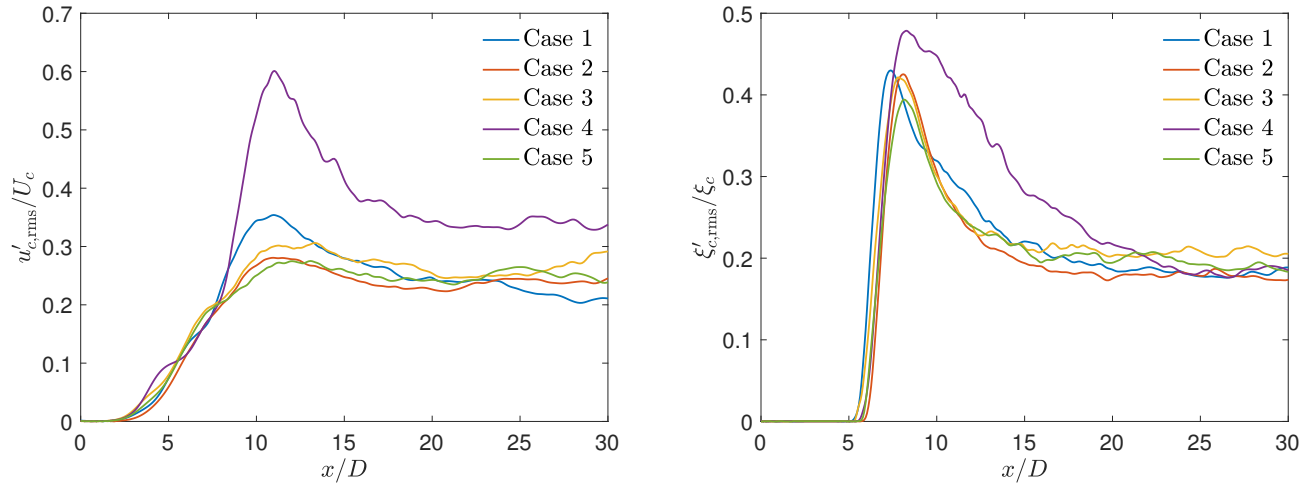

(a) (b)

Fig. 14 Comparison between Cases 1 to 5 of centerline r.m.s. (a) axial velocity fluctuation and (b) scalar fluctuation normalized by the respective centerline values.

[4] Freund, J. B., Lele, S. K., and Moin, P., "Compressibility effects in a turbulent annular mixing layer. Part 1. Turbulence and growth rate," *Journal of Fluid Mechanics*, Vol. 421, 2000, pp. 229–267.

[5] Pantano, C., and Sarkar, S., "A study of compressibility effects in the high-speed turbulent shear layer using direct simulation," *Journal of Fluid Mechanics*, Vol. 451, 2002, pp. 329–371.

[6] Vreman, A. W., Sandham, N., and Luo, K., "Compressible mixing layer growth rate and turbulence characteristics," *Journal of Fluid Mechanics*, Vol. 320, 1996, pp. 235–258.

[7] Newman, J. A., and Brzustowski, T., "Behavior of a liquid jet near the thermodynamic critical region," *AIAA journal*, Vol. 9, No. 8, 1971, pp. 1595–1602.

[8] Woodward, R., and Talley, D., "Raman imaging of transcritical cryogenic propellants," *34th Aerospace Sciences Meeting and Exhibit*, 1996, p. 468.

[9] H. Mayer, W. O., A. Schik, A. H., Vielle, B., Chauveau, C., G-ograve, I., kalp, Talley, D. G., and Woodward, R. D., "Atomization and breakup of cryogenic propellants under high-pressure subcritical and supercritical conditions," *Journal of Propulsion and Power*, Vol. 14, No. 5, 1998, pp. 835–842.

[10] Oschwald, M., and Schik, A., "Supercritical nitrogen free jet investigated by spontaneous Raman scattering," *Experiments in Fluids*, Vol. 27, No. 6, 1999, pp. 497–506.

[11] Chehroudi, B., Talley, D., and Coy, E., "Visual characteristics and initial growth rates of round cryogenic jets at subcritical and supercritical pressures," *Physics of Fluids*, Vol. 14, No. 2, 2002, pp. 850–861.

[12] Mayer, W., Telaar, J., Branam, R., Schneider, G., and Hussong, J., "Raman measurements of cryogenic injection at supercritical pressure," *Heat and Mass Transfer*, Vol. 39, No. 8-9, 2003, pp. 709–719.

[13] Segal, C., and Polikhov, S., "Subcritical to supercritical mixing," *Physics of Fluids*, Vol. 20, No. 5, 2008, p. 052101.

[14] Roy, A., Joly, C., and Segal, C., "Disintegrating supercritical jets in a subcritical environment," *Journal of Fluid Mechanics*, Vol. 717, 2013, pp. 193–202.

[15] Falgout, Z., Rahm, M., Wang, Z., and Linne, M., "Evidence for supercritical mixing layers in the ECN Spray A," *Proceedings of the Combustion Institute*, Vol. 35, No. 2, 2015, pp. 1579–1586.

[16] Muthukumaran, C., and Vaidyanathan, A., "Mixing nature of supercritical jet in subcritical and supercritical conditions," *Journal of Propulsion and Power*, Vol. 33, No. 4, 2016, pp. 842–857.

[17] Muthukumaran, C., and Vaidyanathan, A., "Initial instability of round liquid jet at subcritical and supercritical environments," *Physics of Fluids*, Vol. 28, No. 7, 2016, p. 074104.

[18] Baab, S., Förster, F., Lamanna, G., and Weigand, B., "Speed of sound measurements and mixing characterization of underexpanded fuel jets with supercritical reservoir condition using laser-induced thermal acoustics," *Experiments in Fluids*, Vol. 57, No. 11, 2016, p. 172.

[19] Baab, S., Steinhausen, C., Lamanna, G., Weigand, B., and Förster, F., "A quantitative speed of sound database for multi-component jet mixing at high pressure," *Fuel*, 2018.

[20] Mi, J., Nobes, D., and Nathan, G., "Influence of jet exit conditions on the passive scalar field of an axisymmetric free jet," *Journal of Fluid Mechanics*, Vol. 432, 2001, pp. 91–125.

[21] George, W. K., and Davidson, L., "Role of initial conditions in establishing asymptotic flow behavior," *AIAA journal*, Vol. 42, No. 3, 2004, pp. 438–446.

[22] Boersma, B., Brethouwer, G., and Nieuwstadt, F., "A numerical investigation on the effect of the inflow conditions on the self-similar region of a round jet," *Physics of fluids*, Vol. 10, No. 4, 1998, pp. 899–909.

[23] Sharan, N., Matheou, G., and Dimotakis, P. E., "Turbulent shear-layer mixing: initial conditions, and direct-numerical and large-eddy simulations," *Journal of Fluid Mechanics*, Vol. 877, 2019, pp. 35–81.

[24] Okong'o, N., Harstad, K., and Bellan, J., "Direct numerical simulations of O2/H2 temporal mixing layers under supercritical conditions," *AIAA journal*, Vol. 40, No. 5, 2002, pp. 914–926.

[25] Harstad, K. G., Miller, R. S., and Bellan, J., "Efficient high-pressure state equations," *AIChE journal*, Vol. 43, No. 6, 1997, pp. 1605–1610.

[26] Sciacovelli, L., and Bellan, J., "The influence of the chemical composition representation according to the number of species during mixing in high-pressure turbulent flows," *Journal of Fluid Mechanics*, Vol. 863, 2019, pp. 293–340.

[27] Poling, B. E., Prausnitz, J. M., O'connell, J. P., et al., *The properties of gases and liquids*, Vol. 5, Mcgraw-hill New York, 2001.

[28] Lemmon, E. W., Huber, M. L., McLinden, M. O., et al., "NIST standard reference database 23," *NIST reference fluid thermodynamic and transport properties—REFPROP, Version*, Vol. 9, 2010, p. 55.

[29] Bodony, D. J., "Analysis of sponge zones for computational fluid mechanics," *Journal of Computational Physics*, Vol. 212, No. 2, 2006, pp. 681–702.

[30] Poinsot, T. J., and Lele, S., "Boundary conditions for direct simulations of compressible viscous flows," *Journal of computational physics*, Vol. 101, No. 1, 1992, pp. 104–129.

[31] Lodato, G., Domingo, P., and Vervisch, L., "Three-dimensional boundary conditions for direct and large-eddy simulation of compressible viscous flows," *Journal of Computational Physics*, Vol. 227, No. 10, 2008, pp. 5105–5143.

[32] Michalke, A., "Survey on jet instability theory," *Progress in Aerospace Sciences*, Vol. 21, 1984, pp. 159–199.

[33] Klein, M., Sadiki, A., and Janicka, J., "A digital filter based generation of inflow data for spatially developing direct numerical or large eddy simulations," *Journal of computational Physics*, Vol. 186, No. 2, 2003, pp. 652–665.

[34] Lund, T. S., Wu, X., and Squires, K. D., "Generation of turbulent inflow data for spatially-developing boundary layer simulations," *Journal of computational physics*, Vol. 140, No. 2, 1998, pp. 233–258.

[35] Eggels, J., Unger, F., Weiss, M., Westerweel, J., Adrian, R., Friedrich, R., and Nieuwstadt, F., "Fully developed turbulent pipe flow: a comparison between direct numerical simulation and experiment," *Journal of Fluid Mechanics*, Vol. 268, 1994, pp. 175–210.

[36] Sharan, N., and Bellan, J. R., "Numerical aspects for physically accurate Direct Numerical Simulations of turbulent jets," *AIAA Scitech 2019 Forum*, 2019, p. 2011.

[37] Lubbers, C., Brethouwer, G., and Boersma, B., "Simulation of the mixing of a passive scalar in a round turbulent jet," *Fluid Dynamics Research*, Vol. 28, No. 3, 2001, p. 189.

[38] Wygnanski, I., and Fiedler, H., "Some measurements in the self-preserving jet," *Journal of Fluid Mechanics*, Vol. 38, No. 3, 1969, pp. 577–612.

[39] Panchapakesan, N., and Lumley, J., "Turbulence measurements in axisymmetric jets of air and helium. Part 1. Air jet," *Journal of Fluid Mechanics*, Vol. 246, 1993, pp. 197–223.

[40] Hussein, H. J., Capp, S. P., and George, W. K., "Velocity measurements in a high-Reynolds-number, momentum-conserving, axisymmetric, turbulent jet," *Journal of Fluid Mechanics*, Vol. 258, 1994, pp. 31–75.

[41] George, W. K., "The self-preservation of turbulent flows and its relation to initial conditions and coherent structures," *Advances in turbulence*, Vol. 3973, 1989.